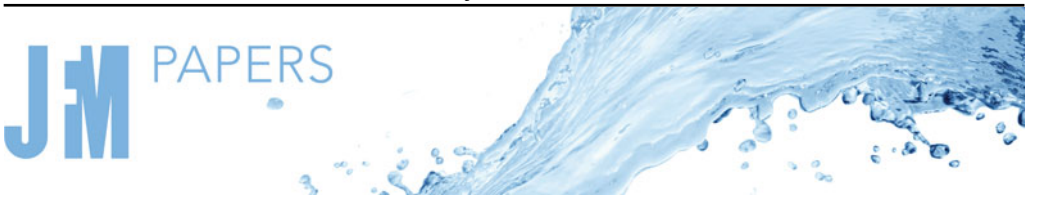
J. Fluid Mech. (2025), *vol.* 1019, A52, doi:10.1017/jfm.2025.10587



Explicit theory of moving contact lines

Jun Luo[1] **and Peng Gao**[1]

[1]Department of Modern Mechanics, University of Science and Technology of China, Hefei, Anhui 230026, PR China

Corresponding author: Peng Gao, gaopeng@ustc.edu.cn

(Received 20 February 2025; revised 27 July 2025; accepted 14 August 2025)

The interface shape near a moving contact line is described by the Cox–Voinov theory, which contains a constant term that is not trivially obtained. In this work, an approximate expression of this term in explicit form is derived under the condition of a Navier slip. Introducing the approximation of a local slippery wedge flow, we first propose a novel form of the generalised lubrication equation. A matched asymptotic analysis of this equation yields the Cox–Voinov relation with the constant term expressed in elementary functions. For various viscosity ratios and contact angles, the theoretical predictions are rigorously validated against full numerical solutions of the Stokes equations and available asymptotic results.

Key words: contact lines, lubrication theory

1. Introduction

The presence of moving contact lines poses a continuing challenge to the study of dynamic wetting. Conventional hydrodynamic descriptions employing no-slip conditions generate non-integrable stress singularities at the contact line (Huh & Scriven 1971), necessitating the incorporation of nanoscale physics for regularisation (Bonn *et al.* 2009; Snoeijer & Andreotti 2013). Among others, the Navier-slip condition emerges as a particularly prevalent framework, introducing a slip length parameter λ of typically a few nanometres. For macroscopic capillary phenomena, the wide span of interacting length scales imposes severe computational constraints, as resolving the physically relevant slip length demands extreme mesh refinement near contact lines (Sui, Ding & Spelt 2014). So far, full-scale numerical simulations of wetting flows are limited to two-dimensional situations (Vandre, Carvalho & Kumar 2012; Sprittles 2015; Keeler *et al.* 2022; Ming, Qin & Gao 2023), yet the extension to practical three-dimensional configurations remains prohibitive. A more efficient approach is to resolve the macroscopic flow only, while the flow near the contact line is built into a macroscale model (see Zhang & Gao 2024, and references therein). The performance of this approach relies obviously on an in-depth understanding of the local flows near the moving contact line.

© The Author(s), 2025. Published by Cambridge University Press.

https://doi.org/10.1017/jfm.2025.10587 Published online by Cambridge University Press

The large viscous force gives rise to a significant variation of the interface angle over a tiny region in the vicinity of a moving contact line. The first quantitative analysis of the interface deformation was performed by Voinov (1976), who proposed a relation between the slope angle θ and the contact-line velocity U, revealing the critical role of viscous bending. A more rigorous theory was proposed by Hocking & Rivers (1982) and Hocking (1983), who investigated the spreading of a drop on a substrate. Incorporating the Navier-slip condition and using matched asymptotic expansions for small U, they revealed the presence of three regions of the interface, namely an inner region with significant slip effect, an outer region depending on the macroscale configuration and an intermediate region bridging them. This scenario was generalised by Cox (1986) to a two-phase set-up with arbitrary viscosity ratio R and other models of contact-line regularisation. In particular, Cox (1986) proposed a relation between θ and the arc length s in the intermediate region, known as the Cox–Voinov law

$$g(\theta, R) = g(\theta_m, R) + Ca\left(\ln\frac{s}{L_m} + Q\right), \tag{1.1}$$

where $g(\theta, R)$ is a complicated function given in (4.8), the capillary number Ca is the dimensionless contact-line velocity and θ_m and L_m denote a microscopic angle and length, respectively. The constant Q depends on the specific contact-line model and is important for the accuracy of the relation. For instance, it is believed that the values of Q should be appropriately taken into account to develop efficient numerical algorithms of macroscale simulations (Sui & Spelt 2013; Solomenko, Spelt & Alix 2017; Zhang & Gao 2024), in which a relation between the local dynamic contact angle and the contact-line speed based on (1.1) is usually employed. However, Q is difficult to calculate even for the simple situation of a singe phase coupled with a Navier-slip model (Hocking & Rivers 1982). The present work aims to provide an explicit expression of Q.

The asymptotic analysis mentioned above is based on a simultaneous treatment of the information of both the bulk flow and the interface, and hence a complicated coupling of the Stokes equations and the boundary conditions. Snoeijer (2006) and Chan *et al.* (2013) developed a novel approach to describe moving contact lines by generalising the lubrication theory (Oron, Davis & Bankoff 1997). In this approach, the parallel-flow approximation is replaced by a no-slip wedge flow (Huh & Scriven 1971) such that large interface slopes can be handled. The generalised lubrication (GL) equation has the form (Chan *et al.* 2013)

$$\frac{\mathrm{d}^2\theta}{\mathrm{d}s^2} = -\frac{CaF(\theta, R)}{h(h + c\lambda)}, \tag{1.2}$$

where $F(\theta, R) = \sin^2\theta/g'(\theta, R)$, with a prime denoting the differentiation to θ. Following the structure of the classical lubrication equation, the term $c\lambda$ is introduced to account for the Navier-slip effect, which is absent in the Huh–Scriven solution. The Cox–Voinov relation (1.1) can be reproduced from the GL equation (Snoeijer 2006). Accordingly, we will show in (4.12) that Q and c are connected. Unfortunately, c, and hence Q, is only available for a contact angle of $\theta_e = 90°$ when $R \neq 0$ (Chan *et al.* 2020).

In this work, we develop a new form of the GL equation, which relies on a physically *ad hoc* yet mathematically convenient slip model. Based on this equation, the constant Q in the Cox–Voinov law (1.1) is determined analytically and expressed in elementary functions for a wide range of viscosity ratio and contact angle. The theory is validated against full numerical solutions of the Stokes equation with a Navier-slip model over a wide range of parameters.

https://doi.org/10.1017/jfm.2025.10587 Published online by Cambridge University Press

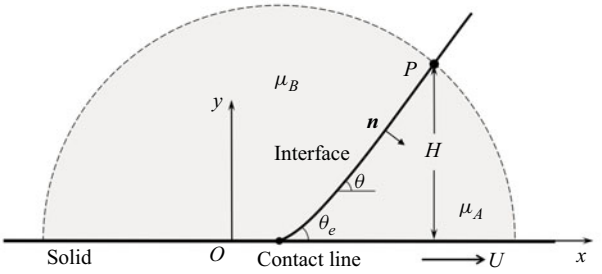


Figure 1. Sketch of the geometry near a moving contact line. The computational domain is shown as the grey region.

2. Model and numerical method

We investigate the local flows in the vicinity of the moving contact line, where the interface of fluid A and fluid B intersects the solid substrate with a microscopic contact angle θ_e, as sketched in figure 1. We adopt the Navier-slip condition to relieve the contact-line singularity and concentrate on the small region with significant slip effect. The motion of the fluids can be treated as a locally two-dimensional Stokes flow where inertial and gravitational forces are neglected. The material parameters of relevance include the viscosities of the fluids, μ_A and μ_B, and the interface tension γ. It is convenient to use a Cartesian reference frame in which the interface evolves into a stationary state, while the substrate is moving at a constant velocity U. The velocity $\boldsymbol{u} = (u_x, u_y)$ and pressure p in each phase are governed by the Stokes equations

$$\boldsymbol{\nabla} \cdot \boldsymbol{u} = 0, \quad -\boldsymbol{\nabla} p + \mu \nabla^2 \boldsymbol{u} = \boldsymbol{0}. \tag{2.1}$$

The velocity satisfies the Navier-slip boundary condition at the substrate

$$u_x - U = \lambda \frac{\partial u_x}{\partial y}, \quad u_y = 0, \tag{2.2}$$

where λ is the slip length. At the fluid–fluid interface, the boundary conditions are

$$\boldsymbol{u}_A = \boldsymbol{u}_B, \tag{2.3}$$

$$\gamma \kappa \boldsymbol{n} = (\boldsymbol{\sigma}_A - \boldsymbol{\sigma}_B) \cdot \boldsymbol{n}. \tag{2.4}$$

Here, $\boldsymbol{\sigma} = -p\boldsymbol{I} + \mu[\boldsymbol{\nabla u} + (\boldsymbol{\nabla u})^T]$ is the stress tensor, $\kappa = \boldsymbol{\nabla} \cdot \boldsymbol{n}$ is the curvature of the interface and $\boldsymbol{n}$ is the unit normal pointing into fluid A. Equations (2.3) and (2.4) represent the continuity of the velocity and tangential stress, while the normal stress has a jump due to the presence of the interface tension. For a general moving or deforming interface, we also require that there is no mass flow across the interface

$$\frac{\mathrm{d}\boldsymbol{x}_i}{\mathrm{d}t} = (\boldsymbol{u}_A \cdot \boldsymbol{n})\boldsymbol{n} = (\boldsymbol{u}_B \cdot \boldsymbol{n})\boldsymbol{n}, \tag{2.5}$$

where $\boldsymbol{x}_i$ represents the location of the interface and t is time. Finally, a contact angle condition is needed at the contact line. For simplicity, we assume that the microscopic contact angle is independent of the contact-line speed and equals the equilibrium contact angle θ_e.

In addition to θ_e, there exist two dimensionless numbers governing the problem, i.e. the capillary number $Ca = \mu_A U/\gamma$ and the viscosity ratio $R = \mu_B/\mu_A$. We focus on the situations of $Ca \ll 1$ such that the interface is weakly deformed.

https://doi.org/10.1017/jfm.2025.10587 Published online by Cambridge University Press

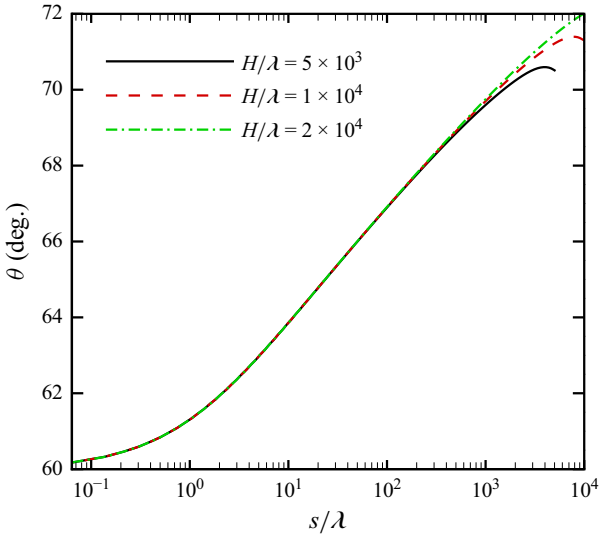


Figure 2. Variation of the slope angle θ as a function of s/λ at $R = 0$, $\theta_e = 60°$, $Ca = 0.01$ and three representative values of the domain size.

Before presenting an approximate theory of moving contact lines, we mention here the computational model to obtain accurate solutions of the full problem, which is important in validating the theoretical results. The flow domain of interest is truncated at a position sufficiently far from the contact line. We employ a semicircular region centred at the contact line as the computational domain, as shown in figure 1. Since the 'far-field' stress should be much smaller than that near the contact line, we set the stress-free condition at the new boundary, i.e. $\boldsymbol{\sigma} \cdot \boldsymbol{n} = 0$. We also impose a vanishing curvature of the interface at the intersection P. These conditions are expected to have no influence on the local wetting flow as long as the domain size is sufficiently large. To obtain a steady solution, the position of P is fixed. The size of the domain can be determined by adjusting the distance between P and the substrate, denoted by H.

The governing equations in (2.1) together with the boundary conditions are solved using a boundary element method (BEM). This method has exhibited the ability to realise full-scale simulations of dynamic wetting with extremely small slip lengths, as demonstrated recently in bubble spreading (Ming *et al.* 2023) and dip coating (Zhang & Gao 2024). The details of the numerical algorithm can be found in Ming *et al.* (2023). Starting from a flat interface with an inclination angle θ_e, the flow eventually evolves into a steady state. Figure 2 shows the steady solution of the interface slope angle θ as a function of the rescaled arc length s/λ. Three representative sizes of the computational domain are selected, corresponding to $H/\lambda = 5 \times 10^3$, 1×10^4 and 2×10^4. It is seen that the numerical results away from the outer boundary can hardly be distinguished as H/λ increases. The numerical results presented hereafter were calculated at $H/\lambda = 1 \times 10^4$, giving reliable comparison at s/λ up to $O(10^3)$.

3. Generalised lubrication theory based on slippery wedge flows

The original form of the GL equation (Snoeijer 2006; Chan *et al.* 2013) relies on the approximation of the local flow by the no-slip wedge flow (Huh & Scriven 1971). We present alternatively a similarity solution of a slippery wedge flow, which can be used to approximate the local flow and to further develop an explicit form of the GL theory.

https://doi.org/10.1017/jfm.2025.10587 Published online by Cambridge University Press

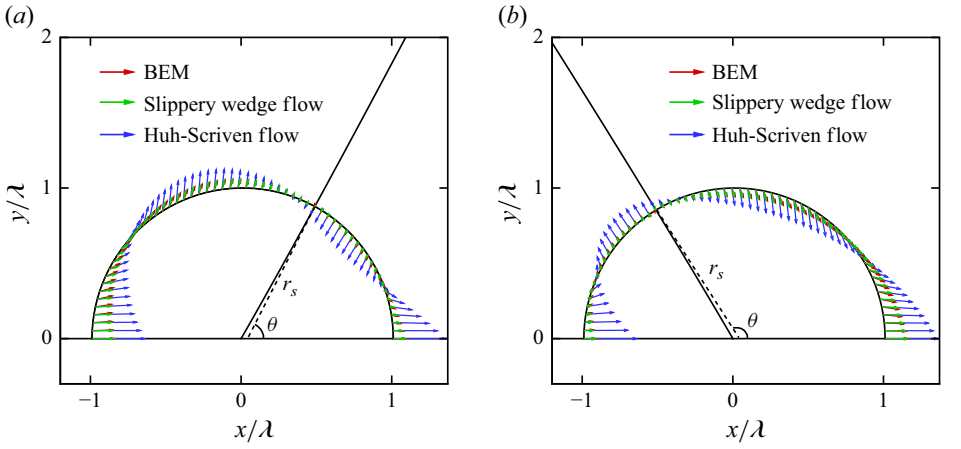


Figure 3. Comparison of the velocity profile at $R = 1$, $Ca = 0.005$, $r_s/\lambda = 1$ and $\theta_e = 60°$ in (*a*) and 120° in (*b*). The slippery wedge flow represents (3.7) and (3.8) with $\beta = \lambda/r_s = 1$ and the Huh & Scriven (1971) solution corresponds to $\beta = 0$.

3.1. *Slippery wedge flow*

As a first approximation, the local geometry can be modelled by a two-phase wedge flow, in which the interface is assumed to be straight and tilted at an angle θ. Introducing the polar coordinates (r, ϕ), the interface is given by $\phi = 0$ and the substrate is given by $\phi = -\theta$ and $\pi - \theta$. In the presence of a Navier slip, Hocking (1977) showed that closed-form solutions are not available. In contrast, we propose a similarity solution of the wedge flow by introducing a linearly varying slip length

$$\lambda = \beta r, \tag{3.1}$$

where β is constant. Since this modified condition eliminates the sole length scale in the problem, a similarity solution in analogous to the no-slip case is retrieved. We note that the similarity solution is not the exact solution with a constant slip length and hence is not expected to describe the global flow near a moving contact line; nevertheless, we will show later that the local flow can be well approximated by this solution with β appropriately adjusted using the radius of the local wedge (denoted by r_s in figure 3), while the slip length remains fixed.

It is convenient to introduce the streamfunction Ψ such that

$$u_r = \frac{1}{r}\frac{\partial \Psi}{\partial \phi}, \quad u_\phi = -\frac{\partial \Psi}{\partial r}. \tag{3.2}$$

Then the Stokes equations can be transformed into

$$\nabla^4 \Psi = 0, \tag{3.3}$$

which is complemented by the boundary conditions

$$\frac{1}{r}\frac{\partial \Psi_A}{\partial \phi} = U + \frac{\beta}{r}\frac{\partial^2 \Psi_A}{\partial \phi^2}, \quad \Psi_A = 0 \quad \text{on} \quad \phi = -\theta, \tag{3.4}$$

$$-\frac{1}{r}\frac{\partial \Psi_B}{\partial \phi} = U + \frac{\beta}{r}\frac{\partial^2 \Psi_B}{\partial \phi^2}, \quad \Psi_B = 0 \quad \text{on} \quad \phi = \pi - \theta, \tag{3.5}$$

$$\Psi_A = \Psi_B = 0, \quad \frac{\partial \Psi_A}{\partial \phi} = \frac{\partial \Psi_B}{\partial \phi}, \quad \frac{\partial^2 \Psi_A}{\partial \phi^2} = R\frac{\partial^2 \Psi_B}{\partial \phi^2} \quad \text{on} \quad \phi = 0. \tag{3.6}$$

https://doi.org/10.1017/jfm.2025.10587 Published online by Cambridge University Press

The solution of (3.3) has the form

$$\Psi_A = Ur\,[M_A\phi\sin(\phi+\theta) + N_A(\phi+\theta)\sin\phi], \tag{3.7}$$

$$\Psi_B = Ur\,[M_B\phi\sin(\phi+\theta-\pi) + N_B(\phi+\theta-\pi)\sin\phi]. \tag{3.8}$$

The coefficients are determined by the boundary conditions (3.4)–(3.6) as

$$\left.\begin{aligned}
M_A &= \{R[f_1(\pi-\theta) - (2\beta+\pi)f_2(\pi-\theta) + 2\beta(\pi-2\theta)\sin^2\theta] \\
&\quad - f_1(\pi-\theta) - 2\beta f_2(\pi-\theta)\}/\Delta, \\
N_A &= -\cos\theta\{R[2\beta f_2(\pi-\theta) - f_3(\pi-\theta) - (4\beta+\pi)\tan\theta - 4\beta(\pi-\theta)] \\
&\quad - f_1(\pi-\theta) - 2\beta f_2(\pi-\theta)\}/\Delta, \\
M_B &= \{f_1(\theta) - (2\beta+\pi)f_2(\theta) - 2\beta(\pi-2\theta)\sin^2\theta - R[f_1(\theta) + 2\beta f_2(\theta)]\}/\Delta, \\
N_B &= \cos\theta\{2\beta f_2(\theta) - f_3(\theta) + (4\beta+\pi)\tan\theta - 4\beta\theta - R[f_1(\theta) + 2\beta f_2(\theta)]\}/\Delta,
\end{aligned}\right\} \tag{3.9}$$

where

$$f_1(\theta) = \theta^2 - \sin^2\theta, \quad f_2(\theta) = \theta - \sin\theta\cos\theta, \quad f_3(\theta) = \theta(\pi-\theta) + \sin^2\theta, \tag{3.10}$$

$$\begin{aligned}
\Delta &= R\left[f_1(\theta) + 2\beta f_2(\theta)\right]\left[f_2(\pi-\theta) + 2\beta\sin^2\theta\right] \\
&\quad + \left[f_1(\pi-\theta) + 2\beta f_2(\pi-\theta)\right]\left[f_2(\theta) + 2\beta\sin^2\theta\right].
\end{aligned} \tag{3.11}$$

It can be easily verified that this solution reduces to the no-slip wedge flow given by Huh & Scriven (1971) when $\beta = 0$.

To check how the flow can be approximated by this slippery wedge flow, a comparison with the BEM solution is performed. For an arbitrary point on the interface, a locally tangent wedge can be defined, as shown in figure 3. We then draw a semicircle centred at the wedge tip, which in general is different from the contact line. Denoting the radius of the semicircle as r_s, the value of β is calculated as λ/r_s. This procedure enables us to plot the velocity of the slippery and no-slip wedge flows along the semicircle and to compare with the BEM results. In figure 3, we have selected a point with $r_s = \lambda$, where the slip effect is important. For both $\theta_e = 60°$ and 120°, the slippery wedge flow agrees well with the numerical results, which we believe is attributable to the matching of the local slip length, while significant deviations of the Huh–Scriven solution occur. A more quantitative comparison is illustrated in figure 4, which shows the variation of u_r and u_ϕ as functions of ϕ for $\theta_e = 60°$. We choose three representative locations corresponding to $r_s/\lambda = 1$, 10 and 100. It is seen that the slippery wedge flow captures satisfactorily the BEM results, especially for the radial component of the velocity u_r. When $r_s/\lambda \gg 1$, the slip effect can be neglected and the curves for the slippery wedge flow, the Huh-Scriven flow and the numerical results collapse.

Furthermore, we examine the asymptotic behaviour of the slippery wedge flow as the moving contact line is approached. On the one hand, when β is fixed, it can be shown that both the shear stress $\tau_{r\phi}$ and the pressure p have a r^{-1} singularity as $r \to 0$ due to the vanishing slip length. On the other hand, for the flow with the local approximation, we have $\lambda = \beta r_s$ fixed and hence β diverges since $r_s \approx r$ near the contact line. In this situation, it can be demonstrated that $\Psi \propto Ur/\beta$ and $\boldsymbol{u} \propto U/\beta$, both of which vanish at the contact line as expected. Accordingly, the viscous stress $\tau_{r\phi} \propto \mu U/(\beta r) \approx \mu U/\lambda$ and is regularised. The pressure gradient can be evaluated from the momentum equation as $\partial p/\partial r \propto \mu U/(\beta r^2) \approx \mu U/(\lambda r)$, yielding $p - p_0 \propto (\mu U/\lambda)\ln(r/\lambda)$, where p_0 is a reference pressure; therefore, the pressure still exhibits a logarithmic singularity, which has been known for moving contact lines with a Navier-slip condition (Buckingham, Shearer & Bertozzi 2003; Benilov & Benilov 2015; Sibley *et al.* 2015).

https://doi.org/10.1017/jfm.2025.10587 Published online by Cambridge University Press

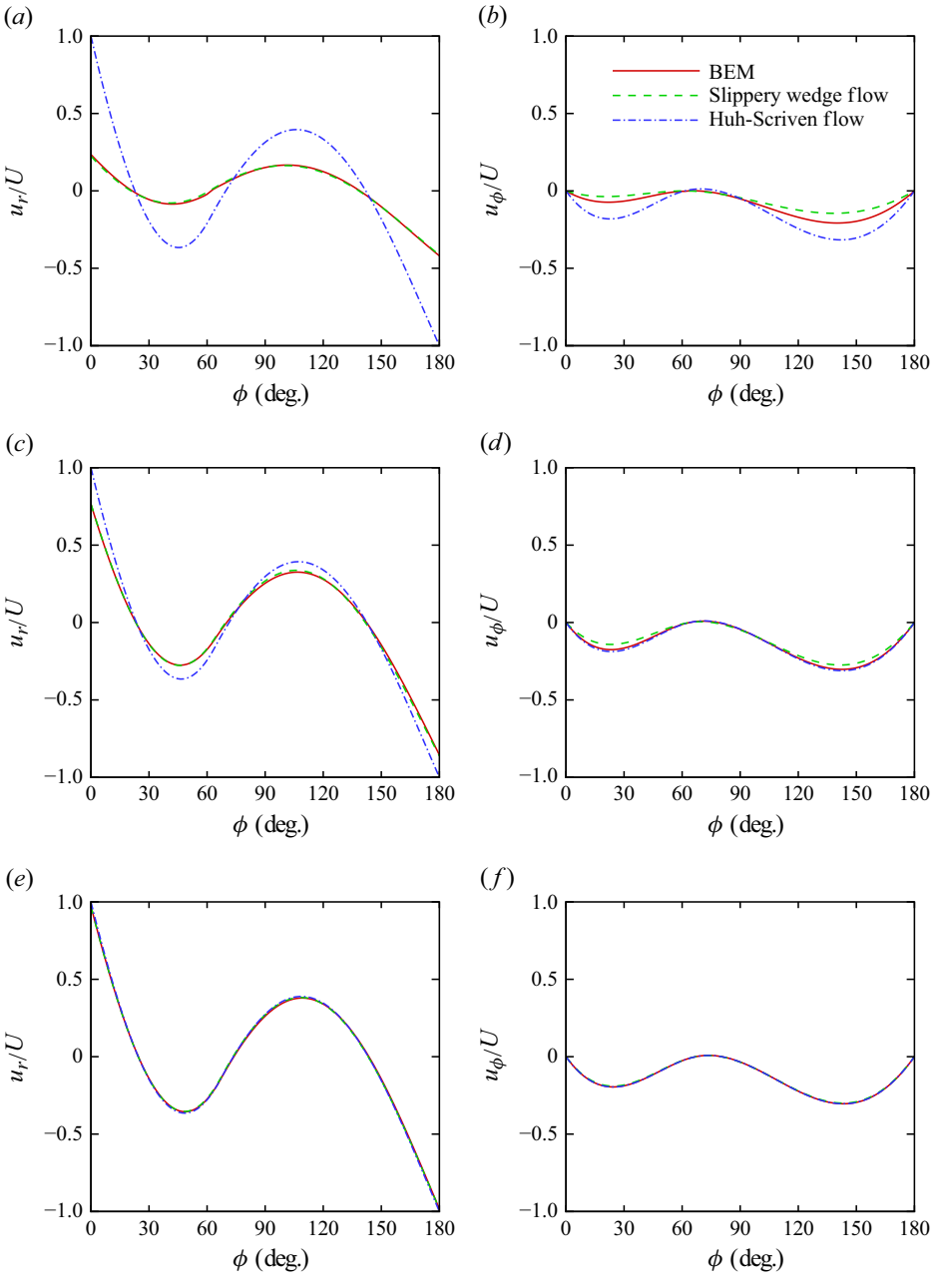


Figure 4. Comparison of the velocity profile at $R = 1$, $Ca = 0.005$ and $\theta_e = 60°$. The slippery wedge flow represents (3.7) and (3.8), and the Huh & Scriven (1971) solution corresponds to $\beta = 0$. The solid lines are produced by BEM with $r_s/\lambda = 1$ (a, b), 10 (c, d) and 100 (e, f). Here, ϕ has been shifted such that the substrate is described by $\phi = 0$ and 180°.

3.2. *Generalised lubrication equation*

We can now derive a novel form of the GL equation, following the procedure of Snoeijer (2006) and Chan *et al.* (2013), but using instead the slippery wedge solution to approximate the local flow. The interface profile is described by $y = h(s)$. Introducing the wedge

https://doi.org/10.1017/jfm.2025.10587 Published online by Cambridge University Press

approximation as in figure 3, we have $r_s = h/\sin\theta$ and hence $\beta = \lambda/r_s = \lambda\sin\theta/h$. The velocity field of this wedge flow can be used to calculate the local stress on the interface, yielding a GL equation for the interface geometry. To this end, the normal component of the dynamic boundary condition (2.4) can be written as

$$\gamma\frac{\mathrm{d}\theta}{\mathrm{d}s} = p_B - p_A, \tag{3.12}$$

where we have used $\kappa = \mathrm{d}\theta/\mathrm{d}s$, and the viscous contribution on the stress can be proved to vanish, similar to the Huh–Scriven flow. Differentiating (3.12) with respect to s and using the momentum equation in (2.1), we have

$$\gamma\frac{\mathrm{d}^2\theta}{\mathrm{d}s^2} = \frac{\partial p_B}{\partial s} - \frac{\partial p_A}{\partial s} = \boldsymbol{e}_s\cdot(\nabla p_B - \nabla p_A) = \boldsymbol{e}_s\cdot\left(\mu_B\nabla^2\boldsymbol{u}_B - \mu_A\nabla^2\boldsymbol{u}_A\right), \tag{3.13}$$

where $\boldsymbol{e}_s$ denotes the unit vector tangent to the interface. The right-hand side of this equation can be calculated using the solution of the slippery wedge flow with β given above. In the local polar coordinates

$$\boldsymbol{e}_s\cdot\nabla^2\boldsymbol{u} = \nabla^2 u_r - \frac{u_r}{r^2} - \frac{2}{r^2}\frac{\partial u_\phi}{\partial\phi} = -2MU\frac{\sin\theta}{r^2} = -2MU\frac{\sin^3\theta}{h^2}. \tag{3.14}$$

Accordingly, (3.13) becomes

$$\frac{\mathrm{d}^2\theta}{\mathrm{d}s^2} = \frac{2Ca\sin^3\theta}{h^2}(M_A + RM_B). \tag{3.15}$$

After substituting (3.9) and making some elementary manipulations, we obtain the GL equation

$$\frac{\mathrm{d}^2\theta}{\mathrm{d}s^2} = -\frac{Ca}{h}\frac{D(\theta,R)h\sin^2\theta + E(\theta,R)\lambda\sin^3\theta}{A(\theta,R)h^2 + B(\theta,R)\lambda h\sin\theta + C(\theta,R)\lambda^2\sin^2\theta}, \tag{3.16}$$

where

$$\left.\begin{aligned}
A(\theta,R) &= Rf_1(\theta)f_2(\pi-\theta) + f_1(\pi-\theta)f_2(\theta),\\
B(\theta,R) &= 2\sin^2\theta[Rf_1(\theta) + f_1(\pi-\theta)] + 2(R+1)f_2(\theta)f_2(\pi-\theta),\\
C(\theta,R) &= 4\sin^2\theta[Rf_2(\theta) + f_2(\pi-\theta)],\\
D(\theta,R) &= 2\sin\theta[R^2f_1(\theta) + 2Rf_3(\theta) + f_1(\pi-\theta)],\\
E(\theta,R) &= 4\sin\theta[R^2f_2(\theta) + R\pi + f_2(\pi-\theta)].
\end{aligned}\right\} \tag{3.17}$$

The equation is closed by adding the geometry relation

$$\frac{\mathrm{d}h}{\mathrm{d}s} = \sin\theta. \tag{3.18}$$

The interface shape near a moving contact line is thus described by a two-equation system for the unknowns $h(s)$ and $\theta(s)$. Both equations are expressed by elementary functions and free of any fit parameter. More importantly, the effect of slip has been incorporated. The equations are complemented by the boundary conditions

$$h(0) = 0, \quad \theta(0) = \theta_e, \quad \kappa(\infty) = 0. \tag{3.19}$$

Several special forms of the GL equation can be obtained. First, setting $\lambda = 0$ for the no-slip case, we have

$$\frac{\mathrm{d}^2\theta}{\mathrm{d}s^2} = -\frac{2Ca}{h^2}\frac{[R^2f_1(\theta) + 2Rf_3(\theta) + f_1(\pi-\theta)]\sin^3\theta}{Rf_1(\theta)f_2(\pi-\theta) + f_1(\pi-\theta)f_2(\theta)}, \tag{3.20}$$

https://doi.org/10.1017/jfm.2025.10587 Published online by Cambridge University Press

which is the same equation proposed by Chan *et al.* (2013) after correcting a sign error therein. Second, when $R = 0$, (3.16) can be simplified to

$$\frac{\mathrm{d}^2\theta}{\mathrm{d}s^2} = -\frac{CaF(\theta)}{h[h + F(\theta)\lambda]}, \quad \text{with} \quad F(\theta) = \frac{2\sin^3\theta}{\theta - \sin\theta\cos\theta}. \tag{3.21}$$

This equation has the same structure of the GL equation as proposed by Chan *et al.* (2013, 2020), but with the fit parameter c replaced by $F(\theta)$. Moreover, in the limit of small slope angles ($\theta \to 0$), we have $\mathrm{d}x/\mathrm{d}s = \cos\theta \to 1$, $\mathrm{d}h/\mathrm{d}x \to \theta$ and $F(\theta) \to 3$; accordingly, (3.21) reduces to

$$\frac{\mathrm{d}^3h}{\mathrm{d}x^3} = -\frac{3Ca}{h(h + 3\lambda)}, \tag{3.22}$$

which is the conventional lubrication equation with a Navier-slip condition (Hocking 1983).

4. Asymptotic solutions

We derive an explicit expression of Q by an asymptotic analysis of the GL equation (3.16) under the condition $Ca \ll 1$. Since the macroscopic region is not considered, the asymptotic structure consists of two regions depending on the importance of the slip effect, i.e. the inner region of size $O(\lambda)$ and the intermediate region with $h \gg \lambda$.

For small Ca, the inner solution can be expanded as

$$h(s) = s\sin\theta_e + Cah_1(s) + O(Ca^2), \quad \theta(s) = \theta_e + Ca\theta_1(s) + O(Ca^2). \tag{4.1}$$

The leading order simply represents a straight wedge geometry with contact angle θ_e. Linearising (3.16) around this static solution, we have

$$\frac{\mathrm{d}^2\theta_1}{\mathrm{d}s^2} = -\frac{Ds + E\lambda}{s(As^2 + B\lambda s + C\lambda^2)}. \tag{4.2}$$

The solution is derived as

$$\begin{aligned}\theta_1 = {} & \frac{s}{2C\lambda}\left(E\ln\frac{As^2 + B\lambda s + C\lambda^2}{As^2} + \frac{2CD - BE}{\Omega}\ln\frac{2As + B\lambda + \Omega\lambda}{2As + B\lambda - \Omega\lambda}\right) \\ & + \frac{D}{2A}\ln\frac{As^2 + B\lambda s + C\lambda^2}{C\lambda^2} + \frac{BD - 2AE}{2A\Omega}\left(\ln\frac{2As + B\lambda + \Omega\lambda}{2As + B\lambda - \Omega\lambda} - \ln\frac{B + \Omega}{B - \Omega}\right),\end{aligned} \tag{4.3}$$

where we have used the boundary condition $\theta_1(0) = 0$ and suppressed the terms yielding finite curvature at large s. The coefficients $A \sim E$ are given by (3.17) with $\theta = \theta_e$, and $\Omega = \sqrt{B^2 - 4AC}$. It can be verified that $B^2 - 4AC \geqslant 0$ and hence Ω is real. The asymptotic behaviour at $s \gg \lambda$ is obtained as

$$\theta - \theta_e \sim \frac{D}{A}\left(\ln\frac{\mathrm{e}s}{\lambda} + \frac{1}{2}\ln\frac{A}{C} + \frac{2AE - BD}{2D\Omega}\ln\frac{B + \Omega}{B - \Omega}\right)Ca. \tag{4.4}$$

Clearly, the inner solution is not expected to hold as $s \to \infty$ since θ_1 diverges.

In the intermediate region ($h \gg \lambda$), the slip effect can be neglected. The governing equation has been given by (3.20) and is rewritten as

$$\frac{A(\theta, R)}{D(\theta, R)}\frac{\mathrm{d}^2\theta}{\mathrm{d}s^2} = -\frac{Ca}{h^2}\sin^2\theta. \tag{4.5}$$

https://doi.org/10.1017/jfm.2025.10587 Published online by Cambridge University Press

Following Snoeijer (2006), we introduce $h \approx s \sin\theta$ for small Ca. Substituting into the above equation and integrating from s to ∞, we have

$$\frac{A(\theta, R)}{D(\theta, R)}\frac{\mathrm{d}\theta}{\mathrm{d}s} - \int_s^\infty \left(\frac{\mathrm{d}\theta}{\mathrm{d}s}\right)^2 \frac{\mathrm{d}}{\mathrm{d}\theta}\left[\frac{A(\theta, R)}{D(\theta, R)}\right]\mathrm{d}s = \frac{Ca}{s}. \tag{4.6}$$

We anticipate $\mathrm{d}\theta/\mathrm{d}s \sim O(Ca/s)$, thereby the integral is of $O(Ca^2/s)$ and can be neglected. Integrating (4.6) once again, we obtain the Cox–Voinov relation

$$g(\theta, R) = g(\theta_e, R) + Ca\left(\ln\frac{s}{\lambda} + Q\right), \tag{4.7}$$

where

$$g(\theta, R) = \int_0^\theta \frac{A(\varphi, R)}{D(\varphi, R)}\mathrm{d}\varphi, \tag{4.8}$$

is the function first proposed by Cox (1986), and Q is the remaining integral constant.

The constant Q is determined by matching the inner and intermediate solutions. For small deviations of θ from θ_e

$$\theta - \theta_e = \frac{g(\theta, R) - g(\theta_e, R)}{\partial_\theta g(\theta_e, R)} = \frac{D}{A}\left(\ln\frac{s}{\lambda} + Q\right)Ca. \tag{4.9}$$

A comparison of (4.4) and (4.9) yields the central results of the present work

$$Q(\theta_e, R) = \frac{1}{2}\ln\frac{A}{C} + \frac{2AE - BD}{2D\Omega}\ln\frac{B + \Omega}{B - \Omega} + 1. \tag{4.10}$$

In particular, in the presence of a single phase only ($R = 0$)

$$Q(\theta_e, 0) = \ln\frac{\theta_e - \sin\theta_e\cos\theta_e}{2\sin^2\theta_e} + 1, \tag{4.11}$$

which can be alternatively obtained from a similar analysis of the single-phase equation (3.21).

For comparison, the procedure of matched asymptotic expansions can be also applied to the GL equation (1.2). As a result, we obtain

$$Q(\theta_e, R) = \ln\frac{\sin\theta_e}{c(\theta_e, R)} + 1. \tag{4.12}$$

The value of c can be obtained explicitly only under special conditions (Chan *et al.* 2020). When $R = 0$, we have

$$Q = \frac{\theta_e - \sin\theta_e\cos\theta_e}{2\sin^2\theta_e}h_1(\theta_e) + 1, \tag{4.13}$$

which has also been reported by Hocking & Rivers (1982). The function $h_1(\theta_e)$ still needs to be calculated by solving numerically an integral equation. Furthermore, an explicit form for $R \neq 0$ is available for $\theta_e = 90^\circ$ and reads

$$Q = \frac{\pi(\pi^2 - 4)\left[(R-1)^2 h_a + 4Rh_b\right]}{4\pi^2(R+1)^2 - 16(R-1)^2} + 1, \tag{4.14}$$

where $h_a = 4(\gamma_E - \ln 2)/\pi$ and $h_b = -1.539$ with γ_E denoting the Euler constant. (Note that the coefficient of h_b should be 2 rather than $2M$ in (2.15*b*) of Chan *et al.* (2020), which was attribute to a typo in (4.11*b*) of Hocking (1977)).

https://doi.org/10.1017/jfm.2025.10587 Published online by Cambridge University Press

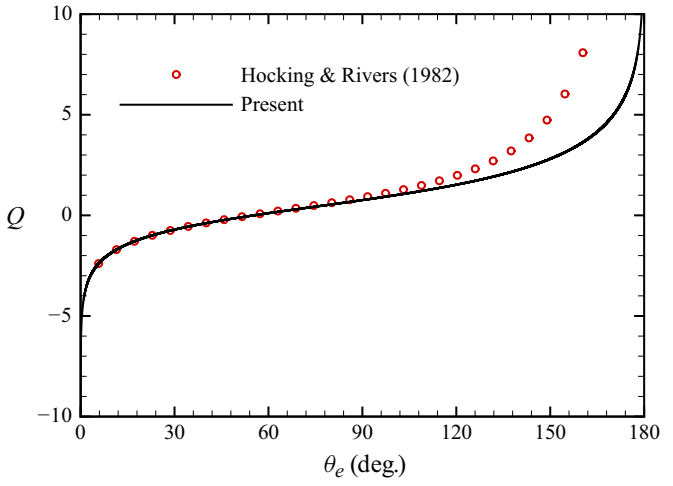


Figure 5. Variation of Q as a function of θ_e for $R = 0$. The solid line denotes the present theory (4.11); the circles represent (4.13) with the values listed in table 1 of Hocking & Rivers (1982). The directory including the data and the Jupyter notebook that generated this figure can be accessed at https://www.cambridge.org/S0022112025105879/JFM-Notebooks/files/figure_5/figure5.ipynb.

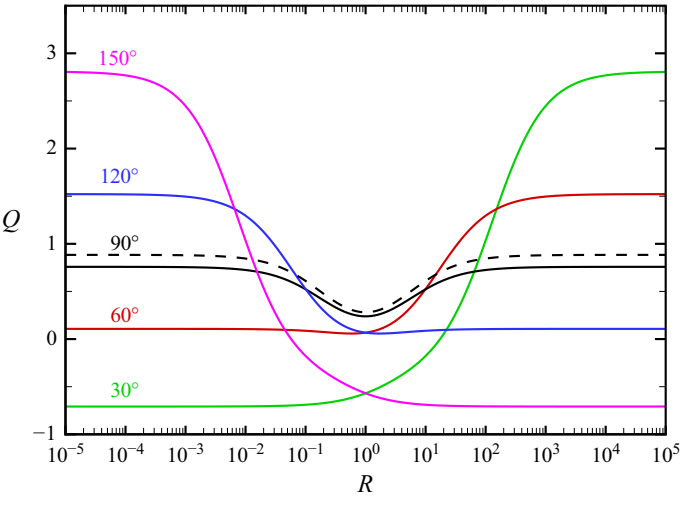


Figure 6. Variation of Q as a function of R for representative values of θ_e. The solid lines denote the present theory (4.10); the dashed line represents (4.14) valid for $\theta_e = 90°$. The directory including the data and the Jupyter notebook that generated this figure can be accessed at https://www.cambridge.org/S0022112025105879/JFM-Notebooks/files/figure_6/figure6.ipynb.

The performance of the present theory is first validated in the presence a single phase ($R = 0$). In this case, the values of Q have been tabulated in Hocking & Rivers (1982), who calculated Q by solving numerically an integral equation. As shown in figure 5, the present theory given by (4.11) agrees well with Hocking & Rivers (1982) when $\theta_e \lesssim 120°$. For larger contact angles, pronounced deviations can be observed. The reason is that the flow near a moving contact line becomes poorly approximated by the slippery wedge flow when the opening angle of the wedge is large. We note that this situation is of less interest since in practice the contact angle is usually less than 120° for a smooth substrate.

Figure 6 shows the behaviour of Q given by (4.10) over a wide range of R and θ_e. It is seen that $Q(\theta_e, R) = Q(\pi - \theta_e, R^{-1})$, which reflects obviously the mirror symmetry of

https://doi.org/10.1017/jfm.2025.10587 Published online by Cambridge University Press

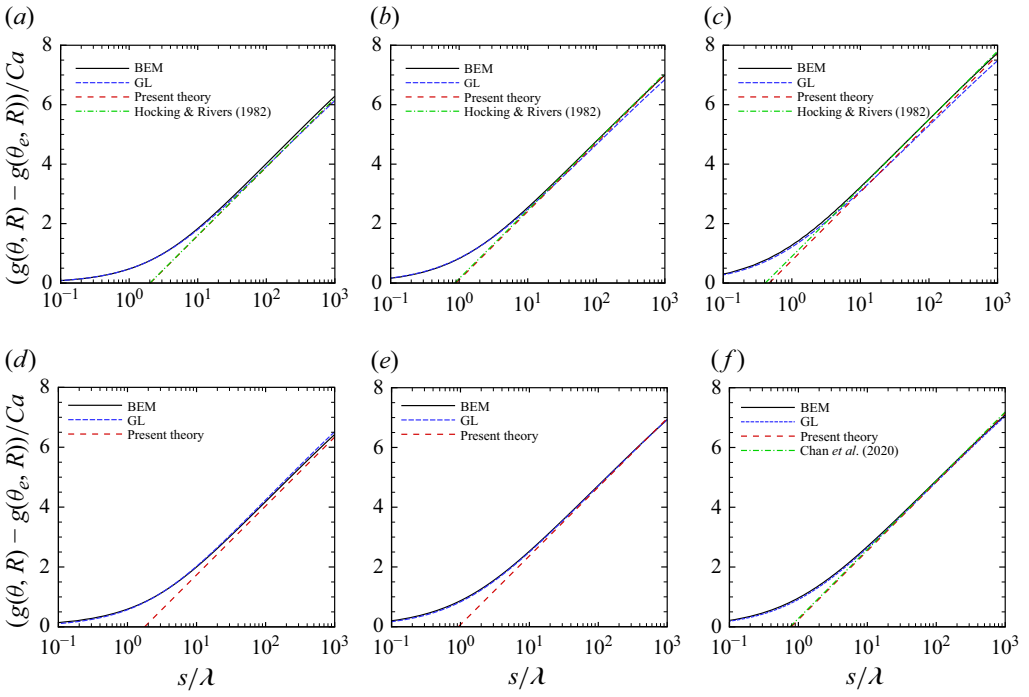


Figure 7. Comparison of the present theory with the BEM results at $Ca = 0.01$: (*a–c*) $R = 0$; (*d–f*) $R = 1$. The contact angles are (*a*, *d*) $\theta_e = 30°$, (*b*, *e*) $\theta_e = 60°$ and (*c*, *f*) $\theta_e = 90°$. The (black) solid curves represent the full numerical results of the BEM. The (blue) dashed curves represent the numerical solutions of the present GL equation (3.16). The (red) long-dashed curves represent the asymptotic solution (4.7) with Q given by (4.10). The (green) dot-dashed curves in (*a–c*) correspond to (4.13), first reported by Hocking & Rivers (1982) and available for $R = 0$ only. The (green) dot-dashed curve in (*f*) corresponds to (4.14), which is based on Chan *et al.* (2020) and valid for $\theta_e = 90°$. The directory including the data and the Jupyter notebook that generated this figure can be accessed at https://www.cambridge.org/S0022112025105879/JFM-Notebooks/files/figure_7/figure7.ipynb.

the set-up. A further comparison can be made at $\theta_e = 90°$ by plotting (4.14) as the dashed line. It is seen that the present theory exhibits an overall underestimation of Q for $\theta_e = 90°$. Nevertheless, the agreement is still satisfactory considering the approximations used in the derivation. It can be shown below that the error of Q does not produce significant deviations from the numerical results of the Stokes equation.

5. Comparison with numerical results

To validate the present GL equation and asymptotic solutions, we show in figure 7 a comparison between the solutions of the GL equation (3.16) and the Stokes equation by plotting the variation of $[g(\theta, R) - g(\theta_e, R)]/Ca$ with s/λ. The results are illustrated for $Ca = 0.01$ together with two viscosity ratios $R = 0$ and 1 and three contact angles $\theta_e = 30°$, $60°$ and $90°$; the employment of different yet small values of Ca produced indistinguishable curves. The numerical solutions of the Stokes equations are obtained by the BEM and represented by the solid curves. The numerical solutions of the GL equation are calculated using a shooting method. The two sets of numerical results exhibits good agreement, especially for $R = 1$.

The Cox–Voinov law is represented by the straight lines, where the values of Q are given by (4.10) for the present theory, (4.13) for $R = 0$ (Hocking & Rivers 1982) and (4.14) for $R = 1$ and $\theta_e = 90°$ (Chan *et al.* 2020). All of the theoretical curves agree

https://doi.org/10.1017/jfm.2025.10587 Published online by Cambridge University Press

reasonably well with the numerical solutions. A close examination of the results show slight deviations in figure 7(*c*, *d*). For $R = 0$ and $\theta_e = 90°$ in figure 7(*c*), the curve of the present asymptotic theory lies below that of Hocking & Rivers (1982), which is due to the underestimation of Q shown in figure 6. This deviation is reduced at $R = 1$, leading to an improved comparison in figure 7(*f*). The slight deviation in figure 7(*d*) is associated with the small contact angle and can be improved at smaller Ca.

6. Concluding remarks

We have developed a similarity solution of a slippery wedge flow, which is found to be a good model to approximate the flow near a moving contact line. Based on this solution, we propose a novel GL equation and an explicit Cox–Voinov theory in the presence of a Navier-slip condition. The presented formulas are applicable to slow contact movement with arbitrary contact angles and viscosity ratios, as demonstrated by a comparison with numerical simulations. The present work significantly complements the study of Hocking & Rivers (1982) and Hocking (1983) for special cases.

For practical purposes, it is of interest to use the Cox–Voinov relation (4.7) to predict the contact-line velocity Ca for given values of $\theta = \theta_d$ at a position far from the contact line, i.e. $s = s_d \gg \lambda$ (Sui & Spelt 2013; Zhang & Gao 2024), according to

$$Ca = \frac{g(\theta_d, R) - g(\theta_e, R)}{\ln(s_d/\lambda) + Q}. \tag{6.1}$$

Compared with the error of Q, of more importance is the relative error of Ca, which can be estimated as

$$\left|\frac{\Delta Ca}{Ca}\right| \approx \left|\frac{\Delta Q}{\ln(s_d/\lambda) + Q}\right|. \tag{6.2}$$

While the error of Q remains notable on the scale of figure 6, one can verify that the error of Ca is very small by retaining the Q term. Taking the case of $R = 0$ and $\theta_e = 90°$ as an example, we have $|\Delta Ca/Ca| \approx 1.6\,\%$ for typically $s_d/\lambda = 10^3$, while the omission of the Q term would yield a much larger error 11.3 %.

In our analysis, macroscopic forces are neglected and can be adopted following Chan *et al.* (2013). For instance, in the presence of a gravity force directing toward positive x, the GL equation can be modified as

$$\frac{\mathrm{d}^2\theta}{\mathrm{d}s^2} = -\frac{Ca}{h}\frac{D(\theta, R)h\sin^2\theta + E(\theta, R)\lambda\sin^3\theta}{A(\theta, R)h^2 + B(\theta, R)\lambda h\sin\theta + C(\theta, R)\lambda^2\sin^2\theta} - \frac{\cos\theta}{l_c^2}, \tag{6.3}$$

where $l_c = \sqrt{\gamma/(\Delta\rho g)}$ is the capillary length defined using the density difference of the fluids $\Delta\rho$ and the gravitational acceleration g.

Supplementary material. Computational Notebook files are available as supplementary material at https://doi.org/10.1017/jfm.2025.10587 and online at https://www.cambridge.org/S0022112025105879/JFM-Notebooks.

Funding. This work was supported by the NSFC (grant nos 12325208, 12241204 and 12388101).

Declaration of interests. The authors report no conflict of interest.

References

Benilov, E.S. & Benilov, M.S. 2015 A thin drop sliding down an inclined plate. *J. Fluid Mech.* **773**, 75–102.

Bonn, D., Eggers, J., Indekeu, J., Meunier, J. & Rolley, E. 2009 Wetting and spreading. *Rev. Mod. Phys.* **81**, 739–805.

https://doi.org/10.1017/jfm.2025.10587 Published online by Cambridge University Press

BUCKINGHAM, R., SHEARER, M. & BERTOZZI, A. 2003 Thin film traveling waves and the Navier slip condition. *SIAM J. Appl. Maths* **63**, 722–744.
CHAN, T.S., KAMAL, C., SNOEIJER, J.H., SPRITTLES, J.E. & EGGERS, J. 2020 Cox–Voinov theory with slip. *J. Fluid Mech.* **900**, A8.
CHAN, T.S., SRIVASTAVA, S., MARCHAND, A., ANDREOTTI, B., BIFERALE, L., TOSCHI, F. & SNOEIJER, J.H. 2013 Hydrodynamics of air entrainment by moving contact lines. *Phys. Fluids* **25**, 074105.
COX, R.G. 1986 The dynamics of the spreading of liquids on a solid surface. Part 1. Viscous flow. *J. Fluid Mech.* **168**, 169–194.
HOCKING, L.M. 1977 A moving fluid interface. Part 2. The removal of the force singularity by a slip flow. *J. Fluid Mech.* **79**, 209–229.
HOCKING, L.M. 1983 The spreading of a thin drop by gravity and capillarity. *Q. J. Mech. Appl. Math.* **36**, 55–69.
HOCKING, L.M. & RIVERS, A.D. 1982 The spreading of a drop by capillary action. *J. Fluid Mech.* **121**, 425–442.
HUH, C. & SCRIVEN, L.E. 1971 Hydrodynamic model of steady movement of a solid/liquid/fluid contact line. *J. Colloid Interface Sci.* **35**, 85–101.
KEELER, J.S., LOCKERBY, D.A., KUMAR, S. & SPRITTLES, J.E. 2022 Stability and bifurcation of dynamic contact lines in two dimensions. *J. Fluid Mech.* **945**, A34.
MING, H., QIN, J. & GAO, P. 2023 Early stage of bubble spreading in a viscous ambient liquid. *J. Fluid Mech.* **964**, A41.
ORON, A., DAVIS, S.H. & BANKOFF, S.G. 1997 Long-scale evolution of thin liquid films. *Rev. Mod. Phys.* **69** (3), 931–980.
SIBLEY, D.N., NOLD, A., SAVVA, N. & KALLIADASIS, S. 2015 A comparison of slip, disjoining pressure, and interface formation models for contact line motion through asymptotic analysis of thin two-dimensional droplet spreading. *J. Eng. Math.* **94**, 19–41.
SNOEIJER, J.H. 2006 Free-surface flows with large slopes: beyond lubrication theory. *Phys. Fluids* **18** (2), 021701.
SNOEIJER, J.H. & ANDREOTTI, B. 2013 Moving contact lines: scales, regimes, and dynamical transitions. *Annu. Rev. Fluid Mech.* **45**, 269–292.
SOLOMENKO, Z., SPELT, P.D.M. & ALIX, P. 2017 A level-set method for large-scale simulations of three-dimensional flows with moving contact lines. *J. Comput. Phys.* **348**, 151–170.
SPRITTLES, J.E. 2015 Air entrainment in dynamic wetting: Knudsen effects and the influence of ambient air pressure. *J. Fluid Mech.* **769**, 444–481.
SUI, Y., DING, H. & SPELT, P.D.M. 2014 Numerical simulations of flows with moving contact lines. *Annu. Rev. Fluid Mech.* **46**, 97–119.
SUI, Y. & SPELT, P.D.M. 2013 An efficient computational model for macroscale simulations of moving contact lines. *J. Comput. Phys.* **242**, 37–52.
VANDRE, E., CARVALHO, M.S. & KUMAR, S. 2012 Delaying the onset of dynamic wetting failure through meniscus confinement. *J. Fluid Mech.* **707**, 496–520.
VOINOV, O.V. 1976 Hydrodynamics of wetting. *Fluid Dyn.* **11**, 714–721.
ZHANG, Z. & GAO, P. 2024 Boundary element simulations of dynamic wetting with a mesoscale contact line model. *Phys. Fluids* **36** (12), 122104.

https://doi.org/10.1017/jfm.2025.10587 Published online by Cambridge University Press